

Solute Segregation in a Moving Grain Boundary: A Novel Phase-Field Approach

Sandip Guin^{a,b,d}, Miral Verma^c, Soumya Bandyopadhyay^a, Yu-Chieh Lo^{*b,d}, Rajdip Mukherjee^{*a},

^aDepartment of Materials Science and Engineering, Indian Institute of Technology, Kanpur, Kanpur-208016, UP, India

^bInternational College of Semiconductor Technology, National Yang Ming Chiao Tung University, Hsinchu 300, Taiwan

^cDepartment of Materials Engineering, KU Leuven, Kasteelpark Arenberg 44, Leuven 3001, Belgium

^dDepartment of Materials Science and Engineering, National Yang Ming Chiao Tung University, Hsinchu 300, Taiwan

Abstract

We present a novel phase-field approach for investigating solute segregation in a moving grain boundary. In our model, the correct choice of various parameters can control the solute-grain boundary interaction potential, resulting in various segregation profiles that agree with Cahn's solute drag theory. Furthermore, we explore how different segregation profiles evolve at varying GB velocities owing to the inequality of the atomic flux of solute between the front and back faces of the moving grain boundary. We highlight velocity variations among segregation profiles in low and high-velocity regimes. This model reveals how grain boundary segregation affects grain growth, providing insights for future alloy design.

Keywords: Grain boundary segregation, solute drag, phase-field model

1. Introduction

Grain boundary (GB) segregation, observed in polycrystalline materials, involves solute atom accumulation in GBs, leading to the stabilization of grain structure [1–4]. For example, solute segregation stabilizes the ultrafine grain structure in cold-sprayed 6061 aluminium powder particles [5]. Segregation reduces grain growth through two mechanisms: (i) solute segregation at GBs lowers GB energy [4, 6, 7], and (ii) solute drag force by GB solute impedes GB migration [8, 9]. Moreover, this solute drag phenomenon in migrating grain boundaries depends on various factors such as grain boundary mobility, solute diffusivity, misfit strain, etc. [10, 11].

Over the last decade, researchers have conducted experimental investigations to quantify GB segregation. *Lejcek et al.* explored temperature-dependent segregation of Sn and Sb in BCC iron GBs, which can be elucidated by both segregation enthalpy and entropy considerations [12]. *Xie et al.* found that Sn segregation in Zircaloy-4 alloys is influenced by the crystallographic orientation [13]. Using first principle approach *Umashankar et al.* studied Y, Zr and Nb segregation in bcc Ti-Mo alloy [14]. Additionally, *Zhang et al.* delved into the mechanisms of phosphorus segregation in steel through the use of Auger electron spectroscopy (AES) [15].

Over recent decades, researchers have proposed numerous theories to quantify grain boundary (GB) segregation [16, 17]. In a comprehensive monograph, *J. W. Cahn* introduced the solute drag theory, elucidating equilibrium GB segregation in both stationary and moving GBs based on solute-GB interaction energy [8]. Cahn's article establishes the relationship between GB velocity and drag force. To explore the influence of segregation

on grain growth kinetics and size distribution, *Fan et al.* employed a phase-field model to simulate grain growth and capture the drag effect [18]. *Heo et al.* investigated the impact of misfit strain on solute-GB interaction using a phase-field model [19].

In existing models, grain boundary solute segregation is typically assumed to be mono-layered [18, 19]. However, recent experimental findings indicate a more intricate phenomenon, with multilayer segregation observed in metallic alloys [20–22]. Moreover, most phase-field simulations regarding the GB segregation assume a symmetrical decrease from the peak solute concentration at the middle of the GB region [19]. This assumption limits their applicability when addressing multilayer GB segregation. A broad spectrum of metallic alloys has been experimentally observed to exhibit multilayer segregation [20, 21]. *Alkayyali et al.* propose a solute drag model based on regular solutions approach, which incorporates the multilayer grain boundary segregation [23]. Their results show that GB-Solute interaction plays significant role in determining solute drag force and multilayer segregation exerts larger drag force than monolayer segregation. *Cahn et al.* showed the solute drag force depends on GB velocity [8]. Thus, to accurately capture the complexities of solute drag on moving grain boundaries at different velocity regime and account for multilayer GB segregation, advanced modeling approaches are crucial.

Thus, in this article, we introduce a novel phase-field model to study various solute segregation patterns at grain boundaries that mimics that multilayer segregation. Phase-field modeling is an elegant computational tool for microstructure modelling without explicit tracking of interfaces [24]. Continuous representation of field variables and a diffuse interface region enable accurate simulation of complex interactions between GBs, surfaces and interphase interfaces. For example, *Mukherjee et al.* employed a phase-field model to study different pathways of

Email addresses: yclo@nycu.edu.tw (Yu-Chieh Lo*), rajdipm@iitk.ac.in (Rajdip Mukherjee*)

microstructure evolution during sintering of nanoporous aggregates for different combinations of surface, GB diffusivity and GB mobility [25]. *Mukherjee et al.* also uses phase field modeling to study GB grooving, revealing anisotropic effects and dynamics [26]. *Verma et al.* investigated grain growth stagnation in solid-state thin films using a phase- field approach, where the surface grooves effectively pin the migrating GBs [27]. In a follow up *Verma et al.* also presented a computational analysis of the time independent behavior of a thermal groove in a migrating GB using a phase- field model [28]. *Suhane et al.* studied the effect of alloying elements in austenite grain growth using phase-field simulations [29].

2. Phase-field model

In this work, we extend the phase-field model proposed by *Heo et al.* modifying the parameter controlling the grain boundary and solute interaction potential [19]. Our phase-field approach employs a conserved order parameter c for solute concentration and a set of non-conserved parameters η_i ; ($i = 1 \dots N$) to represent individual grains in a binary alloy [19]. The total free energy (F) of the system is defined as:

$$F_{total} = \int_V [f_{chem} + c \cdot E + \omega \cdot g(\eta_1, \eta_2, \dots, \eta_g) + \frac{\kappa_c}{2} |\nabla c|^2 + \sum_g \frac{\kappa_\eta}{2} |\nabla \eta_i|^2] dV. \quad (1)$$

Here, f_{chem} represents the chemical free energy density, E represents the chemical interaction between the solute atoms and the grain boundary, and $g(\eta_1, \eta_2, \dots, \eta_g)$ characterizes the local free energy density of the grain structure. The parameter ω is a constant, and κ_c and κ_η are the gradient energy coefficients of composition c and the grain order parameters η_i , respectively. We employ a regular solution-based model to define the f_{chem} in a binary system which is given as,

$$f_{chem} = \mu^0 c + \mu^0_h (1 - c) + RT [c \ln c + (1 - c) \ln (1 - c)] + \Omega c (1 - c). \quad (2)$$

Here, μ^0 and μ^0_h represent the standard chemical potential for solute and host atoms, respectively. R denotes the gas constant, T represents the temperature, and Ω signifies the regular solution interaction parameter. For simplicity, we take Ω to be 0.

The expression for the grain boundary free energy density is given below:

$$g(\eta_1, \eta_2, \dots, \eta_g) = 0.25 + \sum_i \left(-\frac{\eta_i^2}{2} + \frac{\eta_i^4}{4} \right) + \gamma \sum_i \sum_{j>i} \eta_i^2 \eta_j^2, \quad (3)$$

where phenomenological constant γ represents the interactions among the grain order parameter. We take γ to be 1.

We define the solute grain boundary interaction potential E as $-m \cdot \omega \cdot \phi(\eta_1, \eta_2, \dots, \eta_g)$, where the parameter m determines

the strength of the interaction, and $\phi(\eta_1, \eta_2, \dots, \eta_g)$ represents a function derived from the grain structure free energy density $g(\eta_1, \eta_2, \dots, \eta_g)$. Moreover, $\phi(\eta_1, \eta_2, \dots, \eta_g)$ is defined as:

$$\phi(\eta_1, \eta_2, \dots, \eta_g) = \frac{A \left[\left| 1 - \{B(|C \cdot x - 0.5|)\}^N \right| + 1 - \{B(|C \cdot x - 0.5|)\}^N \right] + 2}{R} - D. \quad (4)$$

The parameters A , B , C , D , N , and R mentioned in Eqn (4) exert control over the behavior of $\phi(\eta_1, \eta_2, \dots, \eta_g)$. The correct choice of these parameters provides us with the advantage of controlling the shape of the interaction energy function. Detailed information about all the parameters given in equation 4 is provided in Section 1 of supplementary material. Among them, the only variable is the parameter N in our simulation, as it directly controls the shape of ϕ and consequently influences the shape of E .

In the evolution process, we numerically solve the Cahn-Hilliard equation (Equation 5) for the conserved parameter (c) [30] and the Allen-Cahn equation (Equation 6) for the non-conserved parameter (η_i) [31], given below.

$$\frac{\partial c}{\partial t} = \nabla \cdot M_c \nabla \left(\frac{\partial f_{chem}}{\partial c} - m \cdot \omega \cdot \phi - \kappa_c \nabla^2 c \right), \quad (5)$$

$$\frac{\partial \eta_i}{\partial t} = -L \left(\omega \frac{\partial g}{\partial \eta_i} - m \cdot c \cdot \omega \cdot \frac{\partial \phi}{\partial \eta_i} - \kappa_\eta \nabla^2 \eta_i \right). \quad (6)$$

In these equations, M_c represents the solute's mobility, L is the grain boundary relaxation parameter, and t denotes time. The mobility term M_c is defined as $[M \cdot c(1 - c)]$, where $M = \frac{D}{RT}$ and D represents the interdiffusion coefficient.

The proposed model was implemented using the open-source finite element-based solver MOOSE Framework [32, 33]. We use periodic boundary condition in the X and Y directions. Furthermore, we use Newton's method to solve the governing equations in MOOSE. Note that, the total composition in the entire domain remains conserved through the entire span of the simulations. We employ a computational domain of $4096\Delta X \times 128\Delta Y$ in our phase-field simulations. We set the initial solute concentration (c_0) to 0.1 for all simulations. Table 1 provides the details about the parameters. The simulation details can be found in Section 2 of the supplementary material. Detailed derivation of the governing equations in MOOSE is provided in Section 3 of supplementary material.

3. Results and discussion

We start our study by considering a bicrystal structure featuring a flat stationary GB (as illustrated in Fig 1a). Since the grain boundary is flat, there is no curvature effect, resulting in stationary GB. This is intentional, as our objective is to investigate the segregation profile of the grain boundary for various segregation shapes and validate the results with Cahn's theory. As the values of N change, the interaction potential (E) also varies,

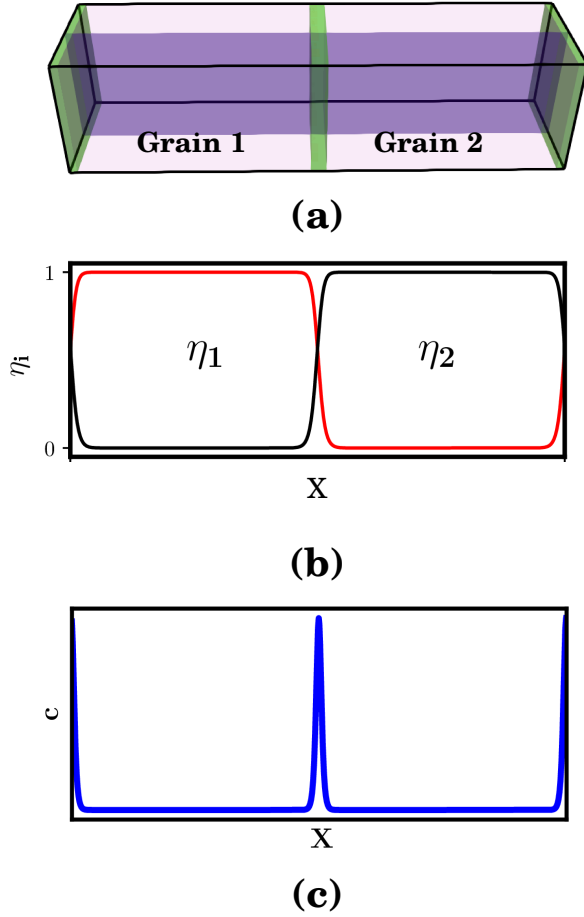


Figure 1: (a) Schematic of a bicrystal system having flat grain boundary of finite thickness. Each grain is represented by light red colored box, while the grain boundary is represented as the green area. (b) Variation of grain order parameter η_i . η_1 represents grain 1 and η_2 represents grain 2. (c) Variation of solute concentration throughout the system.

Parameter	Value
c_o	0.01
m	8.0
κ_η	$1.46 \times 10^{-11} \text{ Jm}^{-1}$
μ^o	$1.08 \times 10^9 \text{ Jm}^{-3}$
μ_h^o	$1.08 \times 10^9 \text{ Jm}^{-3}$
ω	$1.23 \times 10^9 \text{ Jm}^{-3}$
M_c^o	$1.70 \times 10^{-26} \text{ m}^5 \text{ J}^{-1} \text{ s}^{-1}$
L	$2.01 \times 10^{-5} \text{ m}^3 \text{ J}^{-1} \text{ s}^{-1}$
T	655.50 K
σ_{gb}	1.0 Jm^{-2}
l_{gb}	0.9 nm
ΔX	$1.45 \times 10^{-11} \text{ m}$
Δt	$4.57 \times 10^{-5} \text{ s}$

thereby influencing the segregation shapes at the grain boundary. Figures 2(a-d) illustrate the comparison between g and ϕ for various N values: 1, 2, 4, and 10. Clearly, when $N = 1$, both g and ϕ functions are indistinguishable. Nevertheless, with increasing N , the ϕ curve widens symmetrically, leading to a flattened top section. Figures 2(e-h) present the corresponding ratio of solute concentration (c) and matrix solute concentration (c_m) plot at equilibrium and compares with the Cahn Solute Drag (CSD) theory [8]. As the value of N increases, the width of ϕ also broadens (as depicted in Figures 2(a-d)). Consequently, the interaction potential $E = -m \cdot \omega \cdot \phi$ varies with N , affecting the grain boundary's segregation profile. To validate our simulated segregation profile, we compared it with Cahn's equation (Eq 7) for stationary grain boundary as shown :

$$c = c_m \cdot \exp\left\{\frac{-m \cdot \omega \cdot \phi}{RT}\right\}, \quad (7)$$

Our simulation results are consistent with the segregation theory proposed by Cahn [8] grain boundaries. As for stationary GB, the magnitude of flux of solute atoms is identical on both faces of GB, resulting in a symmetrical segregation wrt. the grain GB centre line.

We proceed with simulating various segregation shapes in migrating GB and examining their impact on the solute drag force (P_{drag}). Solute drag force becomes relevant when GB is in motion. However, due to flat GB, the GB remains stationary. To overcome this difficulty, we introduce additional energy $h(\eta_2)$ (given below) in Eq 1 based on the approach proposed by Heo et al. [19]:

$$h(\eta_2) = \beta(-2\eta_2^3 + 3\eta_2^2). \quad (8)$$

Here, β represents the magnitude of the driving force. For $\eta_2 = 0$, $h(\eta_2) = 0$, while for $\eta_2 = 1$, $h(\eta_2) = \beta$. A series of simulations are performed for a range of driving forces ($\beta=0.005$ to 0.030).

For migrating GB, we conduct simulations for both without segregation and with segregation having different shapes ($N=1,2,4$ and 10). Figure 3a illustrates the relationship between the grain boundary velocity (V_{gb}) and the driving force

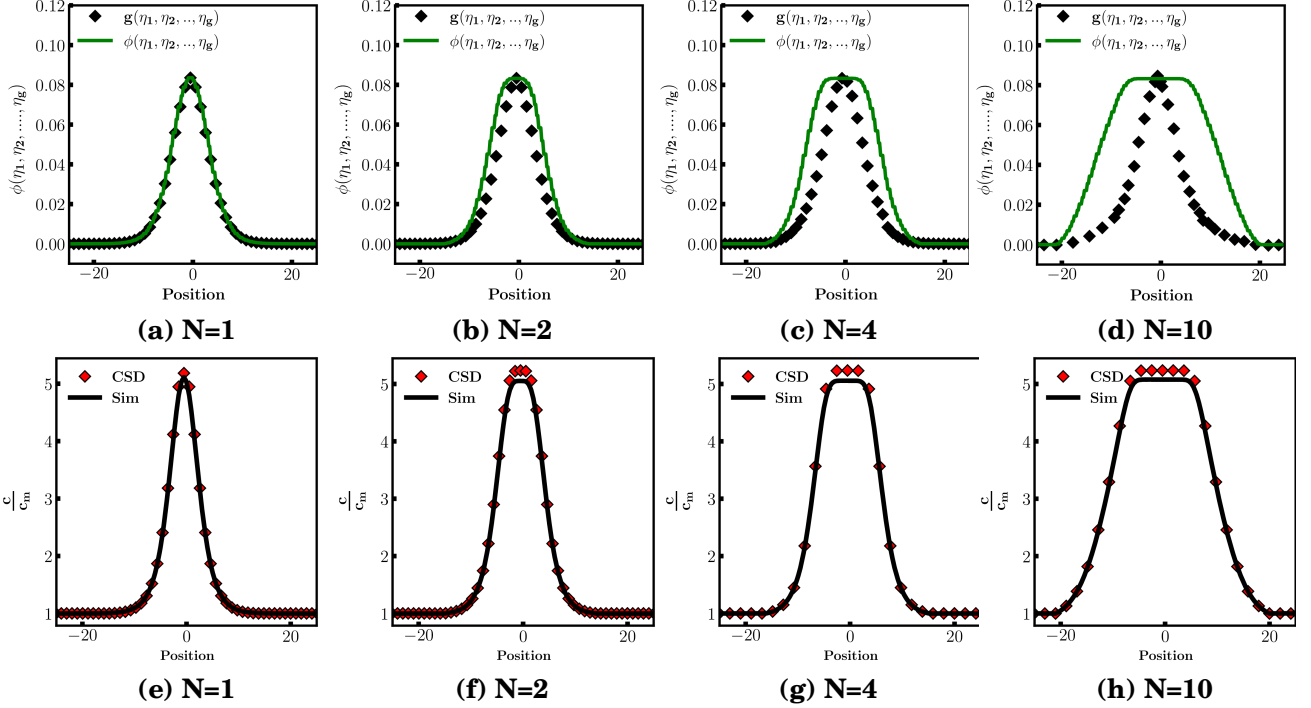


Figure 2: Comparison between $\phi(\eta_1, \eta_2, \dots, \eta_g)$ and $g(\eta_1, \eta_2, \dots, \eta_g)$ for (a) $N=1$, (b) $N=2$, (c) $N=4$ and (d) $N=10$. Simulated composition profile along with Cahn's solute drag theory (CSD) for stationary GB for (e) $N=1$, (f) $N=2$, (g) $N=4$ and (h) $N=10$. Here 'CSD' refers to Equation 7.

(β). The black solid line represents the velocity profile without any grain boundary segregation. The relationship between the grain boundary velocity and the driving force can be expressed as follows:

$$V_{gb} = M_o(\beta - P_{drag}). \quad (9)$$

The equation includes M_o , representing the intrinsic mobility of GB. With no solute segregation ($P_{drag} = 0$), the simplified equation is $V_{gb} = M_o\beta$. In the absence of segregation, GB velocity shows a linear relationship with the driving force, yielding $M_o = 10.9$ in dimensionless units from the slope of the plot.

For grain boundaries (GB) with solute segregation, two distinct velocity regimes emerge: an initial low-velocity regime followed by a later high-velocity regime for all segregation shapes (shown by blue ($N=1$) and red ($N=10$) lines in Figure 3a). The velocity vs. driving force plot for all segregation patterns is given in Section 4 of supplementary material. During the low-velocity regime, $N=1$ exhibits higher velocity than $N=10$. However, in the high-velocity regime, the velocity surpasses a certain point. The velocity crossover between $N=1$ and $N=10$ occurs at $\beta = 0.01765$. After the crossover, $N=1$ exhibits lower velocity than $N=10$. Figure 3(b) shows the comparison between drag force calculated using Eq 9 and Equation 10 [19] for $N=1$ and $N=10$. At low velocity, $N=10$ experiences higher drag force, while at high velocity, it encounters lower drag force compared to $N=1$. The crossover of drag force found to be around $\beta = 0.01765$.

$$P_{drag} = RTV_{gb} \int_{-\infty}^{+\infty} \frac{(c - c_m)}{D(1 - c)} dx. \quad (10)$$

Figure 4(a) displays the composition plot for $N=1$ at various driving forces. A dip in solute concentration is observed in front of the moving grain boundary, consistent with experimental findings [34, 35]. A similar concentration dip is evident for $N=10$ (shown in Figure 4(e)). As the driving force increases, the grain boundary moves faster, making segregation challenging for solute atoms. Thus, peak segregation decreases with higher driving forces in both cases. The intensified driving force accelerates the grain boundary's motion, hindering solute atoms from segregating at GB, as illustrated in Figure 4a and Figure 4e. We compared the segregation profile and CSD [8] theory for migrating grain boundary with constant diffusivity, as described by:

$$D \frac{\delta^2 c}{\delta x^2} + \left\{ \frac{D}{RT} \frac{\delta E}{\delta x} + V_{gb} \right\} \frac{\delta c}{\delta x} + \frac{c}{RT} \left\{ D \frac{\delta^2 E}{\delta x^2} \right\} = 0 \quad (11)$$

Here, the interaction potential term is $-m\omega\phi$. Figure 4(b-d) depicts the comparison of solute concentration between our simulation and the CSD theory (Equation 11) for $N=1$ under different driving forces of 0.010, 0.01765, and 0.030. Figures 4(f-h) depict the comparison of solute concentration between our simulation and the CSD theory (Equation 11) for $N=10$ under different driving forces of 0.010, 0.01765, and 0.030. Our simulation results agrees well with the predictions from the CSD theory for both $N=1$ and $N=10$.

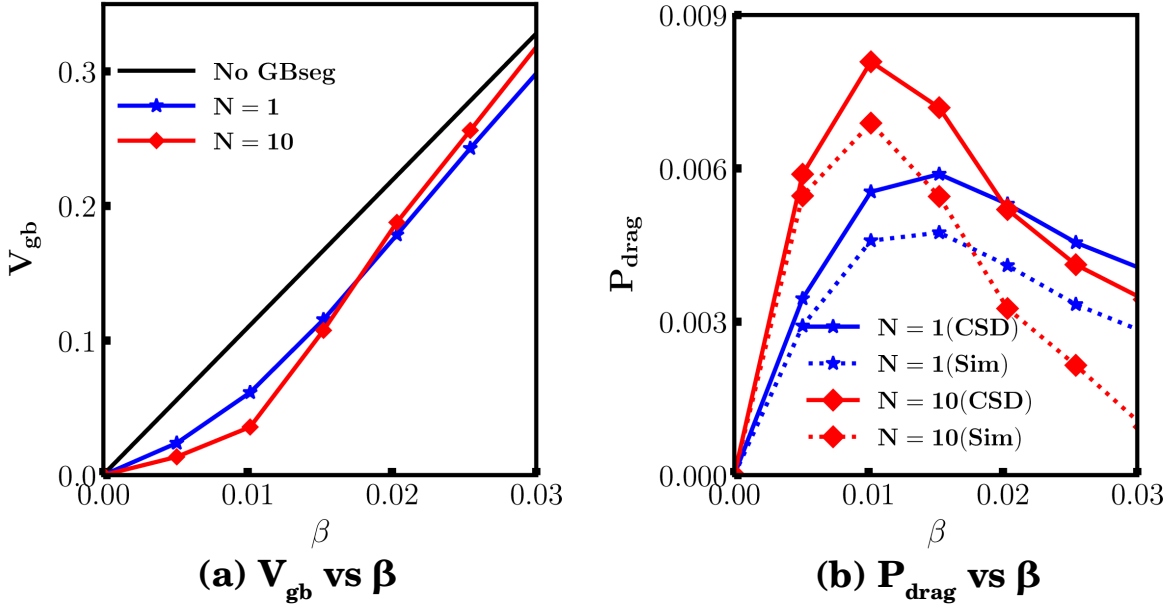


Figure 3: (a) Comparison of velocity (V_{gb}) vs driving force (β) for $N=1$ and 10. (b) Comparison of drag force (P_{drag}) for $N=1$ and 10. Here ‘Sim’ refers to P_{drag} calculation using Equation 9 and ‘CSD’ refers to the calculation using Equation 10.

For values of $N > 1$, indicate the peak segregation occurs across a finite region (shown in Figures 2(f-h)) and the flat region of solute segregations observed for a static GB becomes inclined towards the direction of GB migration. In the case of a stationary GB, solute atoms from the adjacent matrix on both sides of the GB migrate towards it at a same rate, leading to their accumulation at GB. This atomic migration continues until GB segregation reaches a state of equilibrium with matrix. Consequently, the flux on both sides of the grain boundary is equal ($|J_f^-| = |J_f^+|$) where J_f is Fickian flux.

For a moving GB, the amount of segregation diminishes with the increase in the driving force for GB migration, which lowers the peak segregation. The x -component of the total atomic flux with reference to a moving boundary is expressed as $J = J_f - V_{gb} \cdot c$ where the coordinate system is attached to the moving GB and V_{gb} is a positive quantity.

The magnitude of the x -component flux is substantially higher when emanating from the front face of GB, whereas it is comparatively lower from the rear face of GB. In this context, the rear face registers a positive value for J_f due to atom movement directed towards the grain boundary’s center from the rear face (in the positive x -direction). Conversely, the front face presents a negative J_f as atoms migrate in the opposing direction.

Thus, solute atoms undergo longer transportation distances towards the left from the front face, while their motion from the back face is confined to shorter distances towards the right. This results in the accumulation of solute atoms alongside the right side of the back face. Consequently, more segregation of solute atoms adjacent to the back face is evident compared to the front face, leading to a solute concentration gradient within

GB. However, an escalation in the grain boundary migration velocity occurs with an increase in the driving force. This, in turn, reduces the total time required for solute atoms to segregate, leading to a decrease in the overall extent of segregation.

It is observed that the amount of solute segregation decreases with increasing driving force, as shown in Figure 4(e). As the driving force increases, the flux at the front of GB decreases while the flux behind the GB increases. Consequently, the difference in solute concentration between the two faces becomes more pronounced. With further increase in velocity, the flux on the front face approaches zero, resulting in negligible segregation on the front face, as shown in the Figure 4e for $\beta = 0.030$.

Figures 4(i-j) illustrate the comparison of solute concentration profiles for different driving forces of 0.010, 0.01765, and 0.030. Figure 4i focuses explicitly on the driving force of 0.010, representing the pre-crossover stage. In this case, it is evident that the total solute level is higher for $N=10$ compared to $N=1$. For $\beta = 0.01765$ (shown in Figure 4j), the total solute amount is approximately the same for both $N=1$ and $N=10$. However, for $\beta = 0.030$ (shown in Figure 4k), the total solute amount is lower for $N=10$ than $N=1$. The fact that the drag force for a moving grain boundary is a function of $\int_{-\infty}^{+\infty} \frac{(c-c_m)}{D(1-c)}$ justifies the occurrence of the crossover between $N=1$ and $N=10$ under the driving force.

4. Conclusions

We present a novel phase field model for simulating GB segregation, highlighting varied segregation patterns through modified solute-GB interactions. We alter GB segregation profiles by adjusting the parameter of N . For $N > 1$, peak segregation

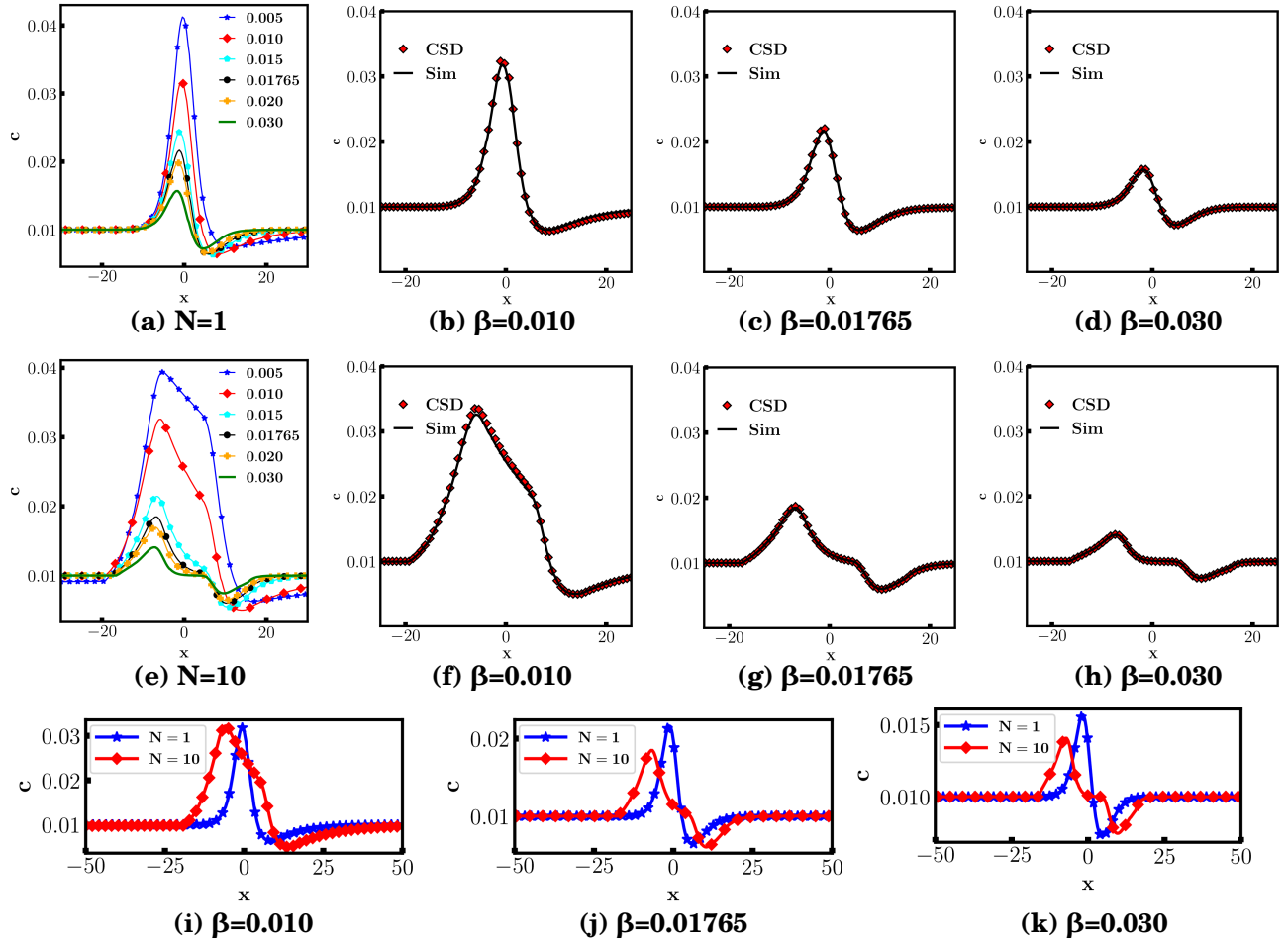


Figure 4: (a) Evolution of grain boundary segregation with driving force (β) for $N=1$. Comparison of segregation profile with Cahn's solute drag theory (CSD) for (b) $\beta = 0.010$, (c) $\beta = 0.01765$ and (d) $\beta = 0.030$, respectively. (e) Evolution grain boundary segregation with driving force (β) for $N=10$. Comparison of segregation with CSD for (f) $\beta = 0.010$, (g) $\beta = 0.01765$ and (h) $\beta = 0.030$, respectively. Comparison of segregation profile between $N=1$ and $N=10$ for (i) $\beta = 0.010$, (j) $\beta = 0.01765$ and (k) $\beta = 0.030$, respectively. Here, 'CSD' refers to calculation using Equation 11.

spans over a finite region. An equal flux of solute atoms from both faces of GB leads to symmetrical solute segregation in stationary GB. However, in the case of a moving GB, the atomic flux is higher at the front face, resulting in more segregation near the back face, establishing a solute concentration gradient within the GB. Increasing driving force escalates GB velocity, reducing solute atoms accumulation time, hence lowering segregation. Additionally, we observe that in the low-velocity regime, $N = 1$ exhibits faster GB velocity than $N > 1$, while the reverse holds in the high-velocity regime. Our phase-field simulations align with Cahn's classical theory on solute drag for both stationary and moving GB.

Acknowledgments

One of the authors R.M. acknowledge financial support from SERB core research grant (CRG/2019/006961). The authors acknowledge National Supercomputing Mission (NSM)

for providing computing resources of 'PARAM Sanganak' at IIT Kanpur, which is implemented by C-DAC and supported by the Ministry of Electronics and Information Technology (MeitY) and Department of Science and Technology (DST), Government of India.

Data Availability Statement

The data that support the findings of this study are available from the corresponding author upon reasonable request.

AUTHOR CONTRIBUTIONS

Sandip Guin: Conceptualization, Visualization, Methodology, Software, Investigation, Formal analysis, Validation, Data curation, Writing-Original Draft. **Miral Verma:** Methodology, Formal analysis, Investigation, Writing-Original Draft.

Soumya Bandyopadhyay : Methodology, Formal analysis, Investigation, Software, Writing-Original Draft. **Yu-Chieh Lo**: Supervision, Project administration, Resources, Writing - review & editing. **Rajdip Mukherjee**: Supervision, Project administration, Resources, Writing - review & editing, Funding acquisition.

References

- [1] Pavel Lejček, Mojmír Šob, and Václav Paidar. Interfacial segregation and grain boundary embrittlement: An overview and critical assessment of experimental data and calculated results. *Progress in Materials Science*, 87:83 – 139, 2017.
- [2] D. Raabe, M. Herbig, S. Sandlöbes, Y. Li, D. Tytko, M. Kuzmina, D. Ponge, and P.-P. Choi. Grain boundary segregation engineering in metallic alloys: A pathway to the design of interfaces. *Current Opinion in Solid State and Materials Science*, 18(4):253 – 261, 2014.
- [3] Paul C. Millett, R. Panneer Selvam, and Ashok Saxena. Stabilizing nanocrystalline materials with dopants. *Acta Materialia*, 55(7):2329–2336, 2007.
- [4] Reiner Kirchheim. Grain coarsening inhibited by solute segregation. *Acta Materialia*, 50(2):413–419, 2002.
- [5] M.R. Rokni, C.A. Widener, and V.R. Champagne. Microstructural stability of ultrafine grained cold sprayed 6061 aluminum alloy. *Applied Surface Science*, 290:482–489, 2014.
- [6] D.A. Aksyonov and A.G. Lipnitskii. Solubility and grain boundary segregation of iron in hcp titanium: A computational study. *Computational Materials Science*, 137:266–272, 2017.
- [7] Yong-Jie Hu, Yi Wang, William Y. Wang, Kristopher A. Darling, Laszlo J. Kecskes, and Zi-Kui Liu. Solute effects on the Σ 3 111[11-0] tilt grain boundary in bcc Fe: Grain boundary segregation, stability, and embrittlement. *Computational Materials Science*, 171:109271, 2020.
- [8] John W Cahn. The impurity-drag effect in grain boundary motion. *Acta Metallurgica*, 10(9):789–798, 1962.
- [9] I. Toda-Caraballo, C. Capdevila, G. Pimentel, and C.G. De Andrés. Drag effects on grain growth dynamics. *Computational Materials Science*, 68:95–106, 2013.
- [10] Malek Alkayyali and Fadi Abdeljawad. Grain boundary solute drag model in regular solution alloys. *Phys. Rev. Lett.*, 127:175503, Oct 2021.
- [11] R. K. Koju and Y. Mishin. The role of grain boundary diffusion in the solute drag effect. *Nanomaterials*, 11(9):2348, Sep 2021.
- [12] P. Lejček, P. Šandera, J. Horníková, J. Pokluda, and M. Godec. On the segregation behavior of tin and antimony at grain boundaries of polycrystalline bcc iron. *Applied Surface Science*, 363:140–144, 2016.
- [13] Shijing Xie, Bangxin Zhou, Chuanming Chen, Boyang Wang, and Dong Jiang. Segregation anisotropy of sn on different crystallographic orientation surfaces of coarse-grained zircaloy-4. *Applied Surface Science*, 363:225–228, 2016.
- [14] Hariharan Umashankar, Daniel Scheiber, Vsevolod I. Razumovskiy, and Matthias Militzer. Modeling solute-grain boundary interactions in a bcc Ti-Mo alloy using density functional theory. *Computational Materials Science*, 229:112393, 2023.
- [15] Xiliang Zhang and Tao Liu. Segregation mechanism of phosphorus in ti-stabilized interstitial-free steel. *Applied Surface Science*, 344:171–175, 2015.
- [16] Pavel Lejček and Siegfried Hofmann. Thermodynamics and structural aspects of grain boundary segregation. *Critical Reviews in Solid State and Materials Sciences*, 20(1):1–85, 1995.
- [17] K Lücke and H.P Stüwe. On the theory of impurity controlled grain boundary motion. *Acta Metallurgica*, 19(10):1087–1099, 1971.
- [18] D Fan, S P Chen, and L Chen. Computer simulation of grain growth kinetics with solute drag. *Journal of Materials Research*, 14(3), 3 1999.
- [19] Tae Wook Heo, Saswata Bhattacharyya, and Long-Qing Chen. A phase field study of strain energy effects on solute-grain boundary interactions. *Acta Materialia*, 59(20):7800–7815, 2011.
- [20] Vivek K. Gupta, Dang-Hyok Yoon, Harry M. Meyer, and Jian Luo. Thin intergranular films and solid-state activated sintering in nickel-doped tungsten. *Acta Materialia*, 55(9):3131–3142, 2007.
- [21] Patrick R. Cantwell, Ming Tang, Shen J. Dillon, Jian Luo, Gregory S. Rohrer, and Martin P. Harmer. Grain boundary complexions. *Acta Materialia*, 62:1–48, 2014.
- [22] Hongbo Xie, Qiuyan Huang, Junyuan Bai, Shanshan Li, Yang Liu, Jianguang Feng, Yuansheng Yang, Hucheng Pan, Hongxiao Li, Yuping Ren, and Gaowu Qin. Nonsymmetrical segregation of solutes in periodic misfit dislocations separated tilt grain boundaries. *Nano Letters*, 21(7):2870–2875, 2021.
- [23] Malek Alkayyali and Fadi Abdeljawad. Grain boundary solute drag model in regular solution alloys. *Phys. Rev. Lett.*, 127:175503, Oct 2021.
- [24] V. Mattos Ferreira, M.G. Mecozzi, R.H. Petrov, and J. Sietsma. Details of pearlite to austenite transformation in steel: Experiments and phase-field modeling. *Computational Materials Science*, 228:112368, 2023.
- [25] Rajdip Mukherjee, Tamoghna Chakrabarti, Erumpukuthickal Ashok Anumol, Thenmathur Appandairajan Abinandanan, and Narayanan Ravishankar. Thermal stability of spherical nanoporous aggregates and formation of hollow structures by sintering—a phase-field study. *ACS Nano*, 5(4):2700–2706, 2011.
- [26] Rajdip Mukherjee and T.A. Abinandanan. Grain boundary grooving in a polycrystalline thin film: A phase-field study. *Computational Materials Science*, 203:111076, 2022.
- [27] M. Verma and R. Mukherjee. Grain growth stagnation in solid state thin films: A phase-field study. *Journal of Applied Physics*, 130(2):025305, 07 2021.
- [28] M. Verma, S. Sugathan, S. Bhattacharya, and R. Mukherjee. A computational analysis of universal behavior of thermal groove in a moving grain boundary. *Scripta Materialia*, 209:114383, 2022.
- [29] Ayush Suhane, Daniel Scheiber, Vsevolod I. Razumovskiy, and Matthias Militzer. Atomistically informed phase field study of austenite grain growth. *Computational Materials Science*, 228:112300, 2023.
- [30] John W Cahn. On spinodal decomposition. *Acta Metallurgica*, 9(9):795–801, 1961.
- [31] Samuel M. Allen and John W. Cahn. A microscopic theory for antiphase boundary motion and its application to antiphase domain coarsening. *Acta Metallurgica*, 27(6):1085–1095, 1979.
- [32] Alexander D. Lindsay, Derek R. Gaston, Cody J. Permann, Jason M. Miller, David Andrić, Andrew E. Slaughter, Fande Kong, Joshua Hansel, Robert W. Carlsen, Casey Icenhour, Logan Harbour, Guillaume L. Giudicelli, Roy H. Stogner, Peter German, Jacob Badger, Sudipta Biswas, Leora Chapuis, Christopher Green, Jason Hales, Tianchen Hu, Wen Jiang, Yeon Sang Jung, Christopher Matthews, Yinbin Miao, April Novak, John W. Peterson, Zachary M. Prince, Andrea Rovinelli, Sebastian Schunert, Daniel Schwen, Benjamin W. Spencer, Swetha Veeraraghavan, Antonio Recuero, Dewen Yushu, Yaqi Wang, Andy Wilkins, and Christopher Wong. 2.0 - MOOSE: Enabling massively parallel multiphysics simulation. *SoftwareX*, 20:101202, 2022.
- [33] D. Schwen, L.K. Aagesen, J.W. Peterson, and M.R. Tonks. Rapid multiphase-field model development using a modular free energy based approach with automatic differentiation in moose/marmot. *Computational Materials Science*, 132:36–45, 2017.
- [34] N. Mavrikakis, W. Saikaly, D. Mangelinck, and M. Dumont. Segregation of Sn on migrating interfaces of ferrite recrystallisation: quantification through apt measurements and comparison with the solute drag theory. *Materialia*, 9:100541, 2020.
- [35] Christopher M. Barr, Stephen M. Foiles, Malek Alkayyali, Yasir Mahmood, Patrick M. Price, David P. Adams, Brad L. Boyce, Fadi Abdeljawad, and Khalid Hattar. The role of grain boundary character in solute segregation and thermal stability of nanocrystalline Pt–Au. *Nanoscale*, 13:3552–3563, 2021.

Supplementary Material

Solute Segregation in a Moving Grain Boundary: A Novel Phase-Field Approach

Sandip Guin^{a,b,d}, Miral Verma^c, Soumya Bandyopadhyay^a, Yu-Chieh Lo^{*b,d}, Rajdip Mukherjee^{*a},

^a*Department of Materials Science and Engineering, Indian Institute of Technology, Kanpur, Kanpur-208016, UP, India*

^b*International College of Semiconductor Technology, National Yang Ming Chiao Tung University, Hsinchu 300, Taiwan*

^c*Department of Materials Engineering, KU Leuven, Kasteelpark Arenberg 44, Leuven 3001, Belgium*

^d*Department of Materials Science and Engineering, National Yang Ming Chiao Tung University, Hsinchu 300, Taiwan*

1. Interaction potential

In our phase-field simulation, we use solute GB interaction potential as $-m\omega\phi$, where ϕ is given by:

$$\phi(\eta_1, \eta_2, \dots, \eta_g) = \frac{A \left[\left| 1 - \{B(|C \cdot x - 0.5|)\}^N \right| + 1 - \{B(|C \cdot x - 0.5|)\}^N \right] + 2}{R} - D. \quad (1)$$

Here the parameters A, B, C, D, N, R are constant. By changing the values of this parameter we can change the shape of the interaction potential, hence the GB segregation shape.

Email addresses: yclo@nycu.edu.tw (Yu-Chieh Lo*), rajdipm@iitk.ac.in (Rajdip Mukherjee*)

7 With an increase in the values of A, the peak value of the function ϕ wrt. g
8 increases while, the lower value of ϕ for same g remains the same. Figures 1(a-
9 c) depict the ϕ vs. g plot, demonstrating how it varies with different A values
10 at N=1 (Figure 1a), N=3 (Figure 1b), and N=10 (Figure 1c). Moreover, as
11 N increases, the upper section of the curve tends to flatten out.

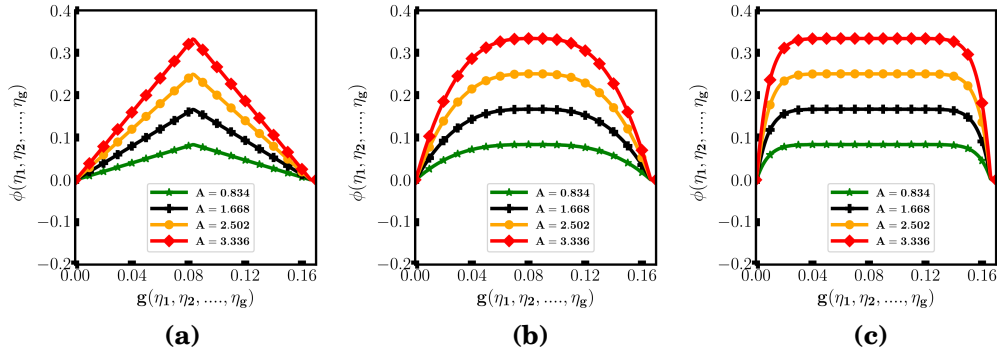


Figure 1: $\phi(\eta_i)$ vs $g(\eta_i)$ plot for different A for (a)N=1, (b)N=3, and (c)N=10.

12 As D values increase, the entire ϕ vs. g plot shifts downwards. Fig-
13 ures 2(a-c) illustrate the variation of the ϕ vs. g plot with different D values
14 for N=1 (Figure 2a), N=3 (Figure 2b), and N=10 (Figure 2c). Additionally,
15 as N increases, the upper section of the curve tends to flatten out, similar to
16 the previous case.

17 As R values increase, the entire ϕ vs. g plot shifts downwards. Fig-
18 ures 3(a-c) illustrate the variation of the ϕ vs. g plot with different R values
19 for N=1 (Figure 3a), N=3 (Figure 3b), and N=10 (Figure 3c). Additionally,
20 as N increases, the upper portion of the curve tends to flatten out, similar
21 to the previous cases.

22 Figures 4 display the variation of ϕ for different values of B and C with

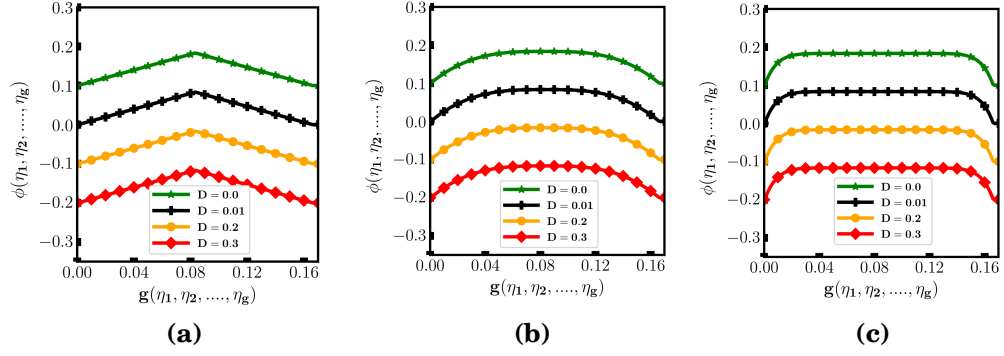


Figure 2: $\phi(\eta_i)$ vs $g(\eta_i)$ plot for different D for (a)N=1, (b)N=3, and (c)N=10.

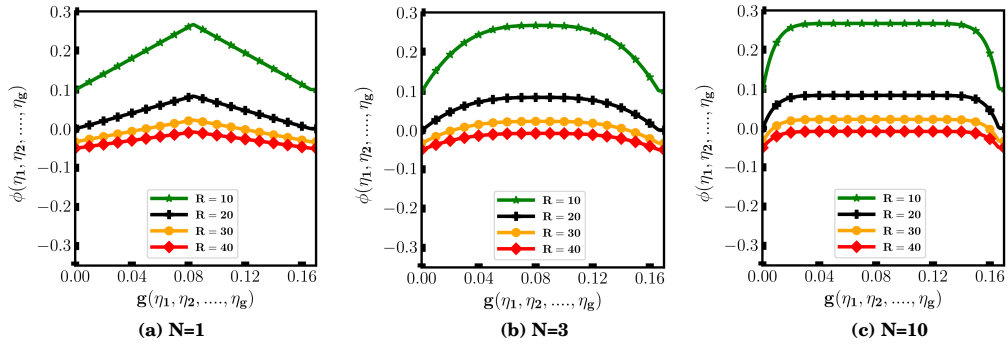


Figure 3: $\phi(\eta_i)$ vs $g(\eta_i)$ plot for different R for (a)N=1, (b)N=3, and (c)N=10.

23 respect to g . In Figure 4(a-c), the curves represent the relationship between
 24 ϕ and g for varying B , $C = 6.0$, $D = 0.1$, $R = 20.0$, and (a) $N = 1$, (b)
 25 $N = 3$, (c) $N = 10$. It is evident that as the value of B increases, the
 26 width of the curve symmetrically expands keeping the centre value at the
 27 same position. An important observation is that the maximum value of ϕ
 28 is located at the center position. However, as the value of C increases, the
 29 ϕ curve shifts towards the left side, maintaining a constant maximum value
 30 (shown in Figures 4(d-f)). Moreover, in both cases, an increase in N causes
 31 the flattening of the upper part of the curve.

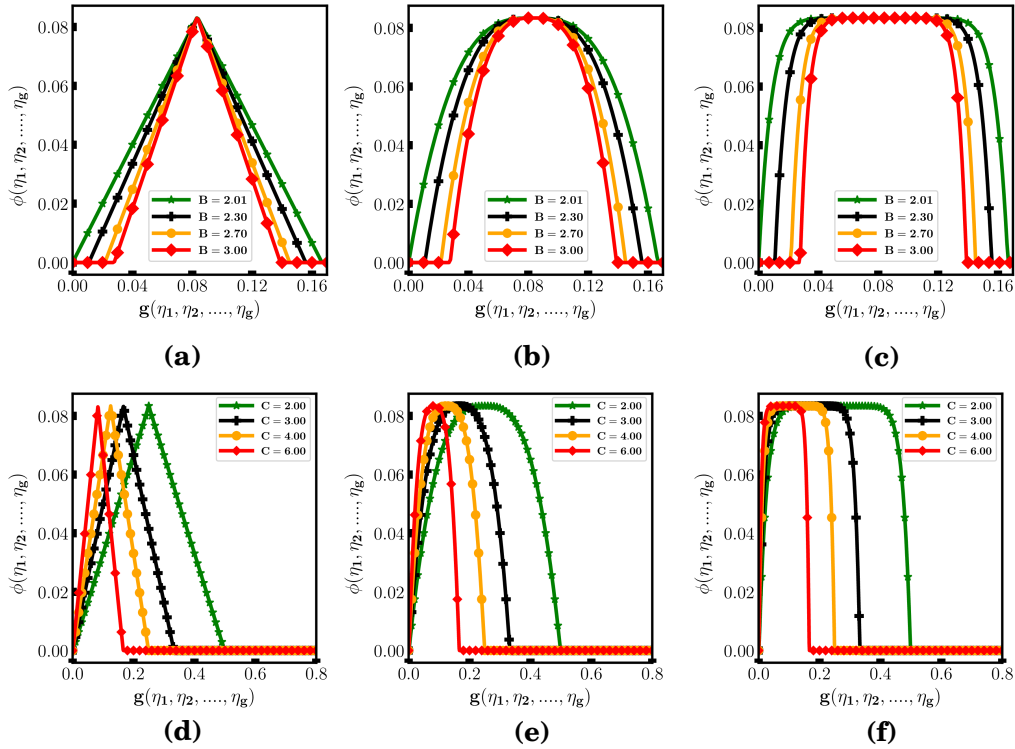


Figure 4: $\phi(\eta_i)$ vs $g(\eta_i)$ plot for different B for (a) $N=1$, (b) $N=3$, and (c) $N=10$. $\phi(\eta_i)$ vs $g(\eta_i)$ plot for different C for (a) $N=1$, (b) $N=3$, and (c) $N=10$.

32 Heo et al. employed E as $-m.\omega.g$ [1] where, the value of g is zero inside
33 the matrix, and gradually increases within GB, and reaches its maximum
34 at the center of the GB. Consequently, the interaction energy in their work
35 follows a similar pattern of variation.

36 In our work, however, we use E as $-m.\omega.\phi$ instead of $-m.\omega.g$, which
37 provides us with greater control over the shape of the interaction energy.
38 Thus, it is crucial to appropriately select all the parameters in such a way
39 that $\phi = 0$ inside the matrix, at the center of the GB, both ϕ and g acquire
40 the same value, and for $N=1$, both functions are identical. For this reason, we
41 choose $B=2.01$, $C=6.0$, $R=20.0$, $A = \frac{R}{2}.g(\eta_1, \eta_2, \dots, \eta_g)|_{x=\text{GB center}}$ and $D =$
42 $\frac{2}{R}$. Furthermore, keeping all the other parameters fixed, we only vary N
43 in our simulation to control the shape of interaction potential function; the
44 shape of GB solute segregation. We observe, as value of N increases, the
45 upper portion of the curve tends to flatten. Figure 5 shows the ϕ vs g plot
46 for different values of N .

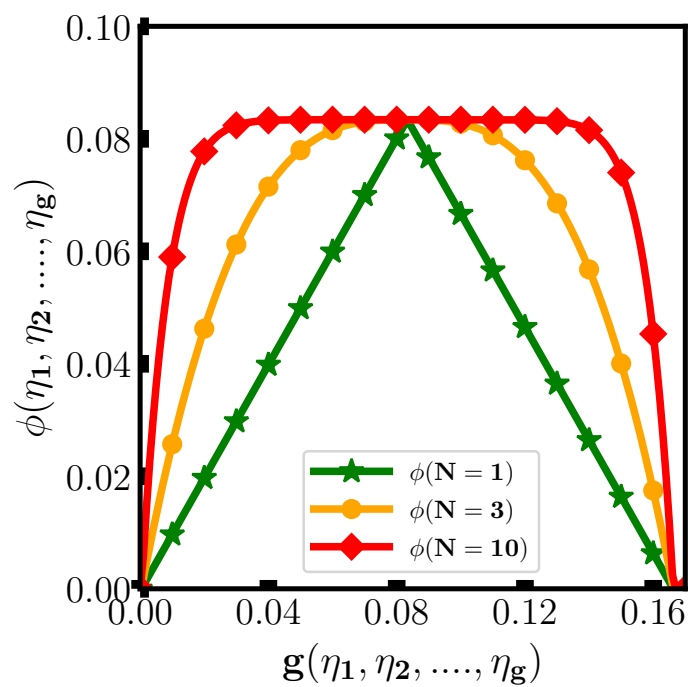


Figure 5: $\phi(\eta_i)$ vs $g(\eta_i)$ plot for $N=1, 3$ and 10 .

47 **2. Simulation details**

48 For our phase-field simulations, we use a computational domain of $4096\Delta X \times$
49 $128\Delta Y$ with periodic boundary conditions in both the X and Y directions.
50 The initial concentration of the solute (c_0) for all simulations was set to 0.1.
51 We considered, the grain boundary energy (σ_{gb}) to be 1.0 Jm^{-2} , and the mea-
52 sured grain boundary width (l_{gb}) as 0.9 nm . The molar volume (V_m) of the
53 material was $11.0 \text{ cm}^3\text{mol}^{-1}$. Please refer to Table 2 for further informa-
54 tion regarding the simulation parameters. We use all the parameters in our
55 simulations in their corresponding non-dimensional form. To perform non-
56 dimensionalization, in our case, the characteristic energy (E_c) is 1.08×10^9
57 Jm^{-3} , and the characteristic length (l_c) is $2.90 \times 10^{-11} \text{ m}$. For a comprehen-
58 sive understanding of the dimensional conversion, we refer to the article by
59 Heo et al [1].

Table 1: Parameters used in phase-field simulations

Parameter	Values
c_o	0.01
m	8.0
κ_η	$1.46 \times 10^{-11} \text{ Jm}^{-1}$
μ^o	$1.08 \times 10^9 \text{ Jm}^{-3}$
μ_h^o	$1.08 \times 10^9 \text{ Jm}^{-3}$
ω	$1.23 \times 10^9 \text{ Jm}^{-3}$
M_c^o	$1.70 \times 10^{-26} \text{ m}^5 \text{ J}^{-1} \text{ s}^{-1}$
L	$2.01 \times 10^{-5} \text{ m}^3 \text{ J}^{-1} \text{ s}^{-1}$
T	655.50 K
σ_{gb}	1.0 Jm^{-2}
l_{gb}	0.9 nm
ΔX	$1.45 \times 10^{-11} \text{ m}$
Δt	$4.57 \times 10^{-5} \text{ s}$

60 **3. Finite element discretization of the governing equations in MOOSE**

61 **Framework**

62 The finite element method (FEM) has been widely used to solve complex
63 partial differential equations (PDE) with ease for many years by the scientific
64 community due to simplicity in the discretization of the equations into the
65 weak form and efficiently handle the exact boundary conditions. Here we
66 perform a FEM-based method to solve the governing phase-field equations
67 (Eqs. (2) & (3)) with periodic boundary conditions,

$$\frac{\partial c}{\partial t} = \nabla \cdot M_c \nabla \left(\frac{\partial f_{chem}}{\delta c} - m \cdot \omega \cdot \phi - \kappa_c \nabla^2 c \right), \quad (2)$$

$$\frac{\partial \eta_i}{\partial t} = -L \left(\omega \frac{\partial g}{\partial \eta_i} - m \cdot c \cdot \omega \cdot \frac{\partial \phi}{\partial \eta_i} - \kappa_\eta \nabla^2 \eta_i \right). \quad (3)$$

68 Solving the Cahn-Hilliard equation is a bit difficult, due to the presence
69 of gradient-free energy which is a fourth-order differential equation. But,
70 it can be solved in two ways. First to prepare for the FEM discretization
71 of Eqn. (2), we construct a weak form in a similar manner to that used
72 by Stogner et al. [2]. The weighted integral residual projection of Eqn. (2)
73 is constructed using a test function ϕ_m and integrating the second-order
74 terms by parts once and the fourth order term by parts twice. Thus after

75 discretization Eqn. (2) yields:

$$\begin{aligned}
\left(\frac{\partial c(\mathbf{r}, t)}{\partial t}, \phi_m \right) &= - \left(\kappa_c \nabla^2 c(\mathbf{r}, t), \nabla \cdot (M_c(c(\mathbf{r}, t), \theta) \nabla \phi_m) \right) \\
&\quad - \left(M_c(c(\mathbf{r}, t), \theta) \nabla \left(\frac{\partial f(c(\mathbf{r}, t))}{\partial c(\mathbf{r}, t)} \right), \nabla \phi_m \right) \\
&\quad + \langle M_c(c(\mathbf{r}, t), \theta) \nabla (\kappa_c (\nabla^2 c(\mathbf{r}, t)) \cdot \hat{n}), \phi_m \rangle \\
&\quad - \left\langle M_c(c(\mathbf{r}, t), \theta) \nabla \left(\frac{\partial f(c(\mathbf{r}, t))}{\partial c(\mathbf{r}, t)} \right) \cdot \hat{n}, \phi_m \right\rangle \\
&\quad + \langle \kappa_c \nabla^2 c(\mathbf{r}, t), M_c(c(\mathbf{r}, t), \theta) \nabla \phi_m \cdot \hat{n} \rangle,
\end{aligned} \tag{4}$$

76 where $(*, *)$ operator represents a volume integral with an inner product and
77 $\langle *, * \rangle$ operator denotes the surface integral with an inner product.

78 Another way to solve Eqn. (2) is to split the fourth order equation into two
79 second order equations, such that two variables are solved, the concentration
80 $c(\mathbf{r}, t)$ and the chemical potential μ . In this case, the two residual equations
81 are:

$$\begin{aligned}
R_\mu &= \left(\frac{\partial c(\mathbf{r}, t)}{\partial t}, \phi_m \right) + (M_c(c(\mathbf{r}, t) \nabla \mu, \nabla \phi_m) \\
&\quad - \langle M_c(c(\mathbf{r}, t) \nabla \mu \cdot \hat{n}, \phi_m \rangle.
\end{aligned} \tag{5a}$$

82

$$\begin{aligned}
R_c &= (\nabla c(\mathbf{r}, t), \nabla (\kappa_c \phi_m)) - \langle \nabla c(\mathbf{r}, t) \cdot \hat{n}, \kappa_c \phi_m \rangle \\
&\quad - \left(\left(\frac{\partial f(c(\mathbf{r}, t))}{\partial c(\mathbf{r}, t)} - \mu \right), \phi_m \right).
\end{aligned} \tag{5b}$$

83 In this work, we mainly adopt the second or the split formalism of Eqn. (5a)
84 & Eqn. (5b) as this change improves the solve convergence without any
85 impact on the solution. In a similar manner, we can also construct the
86 weak form and the corresponding residual for Eq. (3) [3, 4]. For further
87 details related to the weak form please refer to the MOOSE official website
88 <https://mooseframework.inl.gov/>.

89 4. Velocity profiles

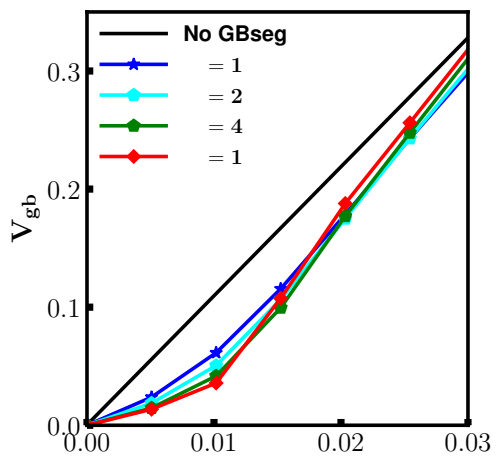


Figure 6: Velocity (V_{gb}) vs. driving force (β) for $N = 1, 2, 4,$ and 10

90 **References**

- 91 [1] Tae Wook Heo, Saswata Bhattacharyya, and Long-Qing Chen. A phase
92 field study of strain energy effects on solute–grain boundary interactions.
93 *Acta Materialia*, 59(20):7800–7815, 2011.
- 94 [2] Roy H Stogner, Graham F Carey, and Bruce T Murray. Approximation
95 of cahn–hilliard diffuse interface models using parallel adaptive mesh re-
96 finement and coarsening with c1 elements. *International journal for nu-
97 merical methods in engineering*, 76(5):636–661, 2008.
- 98 [3] Alexander D. Lindsay, Derek R. Gaston, Cody J. Permann, Jason M.
99 Miller, David Andrš, Andrew E. Slaughter, Fande Kong, Joshua Hansel,
100 Robert W. Carlsen, Casey Icenhour, Logan Harbour, Guillaume L. Giu-
101 dicelli, Roy H. Stogner, Peter German, Jacob Badger, Sudipta Biswas,
102 Leora Chapuis, Christopher Green, Jason Hales, Tianchen Hu, Wen
103 Jiang, Yeon Sang Jung, Christopher Matthews, Yinbin Miao, April No-
104 vak, John W. Peterson, Zachary M. Prince, Andrea Rovinelli, Sebastian
105 Schunert, Daniel Schwen, Benjamin W. Spencer, Swetha Veeraraghavan,
106 Antonio Recuero, Dewen Yushu, Yaqi Wang, Andy Wilkins, and Christo-
107 pher Wong. 2.0 - MOOSE: Enabling massively parallel multiphysics sim-
108 ulation. *SoftwareX*, 20:101202, 2022.
- 109 [4] Michael R Tonks, Derek Gaston, Paul C Millett, David Andrs, and Paul
110 Talbot. An object-oriented finite element framework for multiphysics
111 phase field simulations. *Computational Materials Science*, 51(1):20–29,
112 2012.